

Key role of polar nanoregions in the cubic-to-tetragonal phase transition of potassium-based perovskites

Jacopo Parravicini ^{1,2,3,*} Eugenio DelRe ⁴ Simone Perego ⁵ Maurizio Acciarri ⁵ Simona Binetti ⁵
Yehudit Garcia,⁶ Galina Parapelitsa,⁶ Aharon J. Agranat,⁶ and GianBattista Parravicini⁷

¹Dipartimento di Fisica & Astronomia, Università di Firenze, 50019 Sesto Fiorentino, Italy

²LENS, European Laboratory for Nonlinear Spectroscopy, Università di Firenze, 50019 Sesto Fiorentino, Italy

³CNR-INO, 50019 Sesto Fiorentino, Italy

⁴Dipartimento di Fisica, “Sapienza” Università di Roma, 00185 Rome, Italy

⁵Dipartimento di Scienza dei Materiali, Università di Milano-Bicocca, 20125 Milano, Italy

⁶Applied Physics Department, Hebrew University of Jerusalem, 91904 Jerusalem, Israel

⁷Dipartimento di Fisica, Università di Pavia, 27100 Pavia, Italy

 (Received 23 March 2022; revised 25 June 2022; accepted 1 August 2022; published 22 August 2022)

We investigate samples of compositionally disordered potassium-based perovskite single crystals with different composition and stoichiometry. The dielectric and Raman response is inspected over the nominal cubic-to-tetragonal long-range phase transition. The comparison between results shows that the occurrence of the phase transition is controlled by the temperature evolution of polar nanoregions (PNRs). We are able to correlate PNR order, formation, percolation, and freezing to the characteristic temperatures of each macroscopic crystal. The onset of the phase transition is found to occur when PNRs undergo a percolative ordering process, in correlation to the sudden arising of a specific high-frequency Raman mode.

DOI: [10.1103/PhysRevB.106.064107](https://doi.org/10.1103/PhysRevB.106.064107)

I. INTRODUCTION

Disordered inorganic perovskites have gained great attention due to their interesting and useful optical, magnetic, mechanical, and electric features [1–7]. These peculiar properties are found to be correlated to substitutional disorder and the formation of mesoscopic nanometric polar regions, or *polar nanoregions* (PNRs), at T^* temperature [1,8]. Samples, which are phenomenologically classified as *relaxors* [1], can manifest features typical of dipolar liquids, solids, and even glasses, when the PNRs are highly mobile, fixed, or in a so-called frozen state, respectively [1,8,9]. Furthermore, the observation of a macroscopic polarization response, with specific thresholds as a function of temperature, has been attributed to PNR percolation [10]. Experiments in different compounds using different methods suggested that the ferroelectric transition displays percolative features [10–17]. Complex behavior in the dielectric response is generally addressed introducing a set of phenomenological temperatures that side the Curie temperature in describing the cubic-to-tetragonal transition. One commonly accepted approach is to consider the so-called Burns (T_B), intermediate (T^*), and Curie-Weiss ferroelectric (T_c) transition temperatures [18–20]. This approach has been implemented to describe potassium-based crystals. In particular, the properties of the ferroelectric solid solutions $K_{1-y}Li_yTa_{1-x}Nb_xO_3$ (KLTN) and $K_{1-y}Na_yTa_{1-x}Nb_xO_3$ (KNTN) have been the subject of intense investigation [4,5,21]. KLTN, KNTN, and KTN samples

have shown interesting properties, such as the enhancement of electrooptic response [22,23], scale-free and subwavelength propagation [2,3,24,25], marked order-disorder anisotropies [4,5], programmability and hysteretic effects [26–28], rejuvenation [29], giant broadband refraction [6,30], and peculiar lattice structure [31]. The underlying perovskite geometry of KLTN, KNTN, and KTN makes them a simpler structure compared to lead-based ferroelectric crystals, allowing the response to be interpreted in terms of PNRs [15,32,33]. The structural properties of KLTN and KNTN were investigated in terms of order/disorder features using inelastic light scattering [33], dielectric spectroscopy [4,5,34], and Raman spectroscopy [32,35–39]. The last of these revealed the presence of a PNR-driven nonlinear scattering and a Raman response with Fano resonances [32,39,40]. Results showed that PNRs can strongly influence the interaction between photons and phonons, a complex correlation among microscopic, mesoscopic, and macroscopic scales.

In this work we investigate the behavior of disordered KLTN, KNTN, and KTN single crystals at cubic-to-tetragonal phase transition conditions. The investigation is carried out on four different potassium-based samples: two KLTN crystals, whose different stoichiometry makes one to display a relaxor dielectric response, while the second one has a typical behavior of a canonical ferroelectric; one crystal with sodium (KNTN); and one without a second alkaline ion (KTN). We combine dielectric, order-disorder analysis based on Fröhlich entropy [41–45], and Raman response measurements as a function of temperature in the transition region 260–320 K, in proximity of the Curie point. This approach allows us to associate Raman response to different qualitative evolutions of

*Corresponding author: jacopo.parravicini@unifi.it

the PNRs whose formation, dissolution, and changes identify the different characteristic temperatures which are associated to the cubic-to-tetragonal phase transition.

A common feature in all samples is the sudden appearance of a Raman mode at 830 cm^{-1} at the temperature for which the dielectric response peaks. These findings indicate the existence of what we call the *transition mode*, strictly linked to a PNR percolation that then forms the physical underpinning of the transition.

II. EXPERIMENTAL SETUP AND TECHNIQUES

Experiments are performed in four single crystals of potassium tantalate-niobate. Two of them, labeled KLTN1 and KLTN2, are lithium-enriched single crystals ($\text{K}_{1-y}\text{Li}_y\text{Ta}_{1-x}\text{Nb}_x\text{O}_3$), with $x = 0.36$, $y = 0.003$, and $x = 0.36$, $y = 0.013$, respectively; one sample, KNTN, is sodium-enriched ($\text{K}_{1-y}\text{Na}_y\text{Ta}_{1-x}\text{Nb}_x\text{O}_3$), with $x = 0.37$, $y = 0.15$; the last one, KTN, has composition $\text{KTa}_{1-x}\text{Nb}_x\text{O}_3$ with $x = 0.36$. All samples were grown through the top-seeded-solution method [21]. The investigated samples are *c*-direction-pulled zero-cut, measuring $3.78(a) \times 3.55(b) \times 2.03(c)\text{ mm}^3$ KLTN1, $3.00(a) \times 2.05(b) \times 1.05(c)\text{ mm}^3$ KLTN2, $2.85(a) \times 2.94(b) \times 2.80(c)\text{ mm}^3$ KNTN [5], and $1.80(a) \times 1.80(b) \times 2.30(c)\text{ mm}^3$ KTN, with the largest facets perpendicular to the [100] direction. The concentration of each chemical element in the samples is determined by electron microprobe analysis. To obtain Raman spectra, the largest (100) facets were polished to optical grade.

The real part of the relative dielectric permittivity $\epsilon_r = \epsilon_r(T)$ is measured as a function of the temperature T using a high-precision LCR meter (Agilent-4284A with a probing field of 1 V/cm). The temperature is varied using a T -controlled closed two-stages helium cryostat in a vacuum configuration and monitored through a calibrated silicon diode sensor (0.01 K in precision). The T variation rate is 1 K/min and the system records one value until a 0.25 K variation is detected. The measurements were performed for the frequencies 10, 100, and 1000 kHz, where the condition required by relationship of Eq. (36) of [44] is satisfied. A sample temperature is set in the 260–320 K range: therein, the nominal cubic-to-tetragonal phase transition can be found [4,5], as also confirmed by, e.g., temperature-resolved microscopic x-ray-diffractometry measurements [31].

The evolution of the sample state-of-order as a function of temperature is analyzed using Fröhlich entropy evaluation [44]. This approach exploits the relationship between $\epsilon(T)$ and the entropy variation $S(T)$ induced by an applied electric field E . Under suitable conditions, the entropy $S_{\text{tot}}(T)$ of a dielectric material subject to an external electric field E is given, per volume unit, by [42,44]

$$S_{\text{tot}}(T) = S_0(T) + \frac{\epsilon_0}{2} \frac{\partial \epsilon_r}{\partial T} E^2 = S_0(T) + S(T), \quad (1)$$

where ϵ_0 and ϵ_r are, respectively, the vacuum and the relative dielectric constant while $S_0(T)$ is the field-independent part of the entropy [42]. We define the Fröhlich entropy per unit of volume and electric field as [4,43,44,46]

$$s = \frac{\epsilon_0}{2} \frac{\partial \epsilon_r}{\partial T}, \quad (2)$$

i.e., Eq. (21) by [44]. According to Eq. (2), the application of an electric field increases the entropy if $\partial \epsilon / \partial T$ is positive, while it decreases the entropy when $\partial \epsilon / \partial T$ is negative. As pointed out by Fröhlich, in disordered (dipolar liquid-like) systems an applied electric field creates order since it orients the dipoles otherwise randomly arranged; as a consequence the entropy variation $s(T)$ induced by the field is negative. On the contrary, in dipolar-ordered systems (dipolar solid-like) the field perturbs the established ordered state, so that the field-induced entropy $s(T)$ is positive. In other words, the condition $\partial \epsilon / \partial T < 0$ signals a disordered system while $\partial \epsilon / \partial T > 0$ indicates an ordered state [4,41,42,44,47].

Raman measurements are carried out in a backscattering configuration of a *Jasco Ventuno* μ -Raman system. The instrument is equipped with a cooled charged-coupled device (CCD) camera sensor and an unpolarized pump He-Ne laser (wavelength 632.8 nm, power 8 mW) that illuminates the sample parallel to the crystalline *c*-axis. Three different objectives (namely, $100\times$ with 0.95 NA numerical aperture, $20\times$ with 0.46 NA, and $5\times$ with 0.15 NA) and attenuating filters allow us to carry out Raman measurements with different intensities. In our setup, the best signal-to-noise ratio was found using a $20\times$ 0.46 NA objective, producing a spot diameter of 4 mm. The spectral resolution is set to 1.5 cm^{-1} . Before each measurement the system is calibrated through a single-crystal Si reference, imposing the position of the dominant Si peak at 520.65 cm^{-1} [48,49]. The sample is placed on a Peltier junction in a dry chamber, which is directly connected with the objectives of the Raman spectroscopy system. The Peltier system enables to finely control the temperature of the sample from $T = 265\text{ K}$ to $T = 325\text{ K}$. Each Raman shift intensity measurement $I = I(\nu)$ is carried out at a fixed temperature, where the spectrum is recorded from 88 to 1000 cm^{-1} . The Raman spectra as a function of the temperature is given in terms of the I^r reduced intensity of the Stokes component, with [32,39,40]

$$I^r(\nu) = \frac{I(\nu)}{2\pi\nu n(\nu)}. \quad (3)$$

Here $I(\nu)$ and $n(\nu) = 1 + \exp(-h\nu/K_B T)$ are the observed Raman scattering intensity and the Bose-Einstein population factor, respectively, while h is the Planck constant, K_B is the Boltzmann constant, and T is the temperature. Being that our investigation is aimed at finely investigating the details of the phase transition, we employ a high scan rate of approximately one recorded point for each temperature degree.

III. DIELECTRIC RESPONSE AND FRÖHLICH ENTROPY

In Figs. 1–4 data from dielectric measurements are reported for KLTN1, KLTN2, KNTN, and KTN samples, respectively.

In Fig. 1(a) the real part of the relative permittivity as a function of temperature $\epsilon_r(T)$ of the KLTN1 sample is reported in the 260–320 K range. The peak with the maximum at $T_{c\text{-KLTN1}} \simeq 288\text{ K}$ signals the occurring of a transition from cubic (high T) to tetragonal (low T) long-range

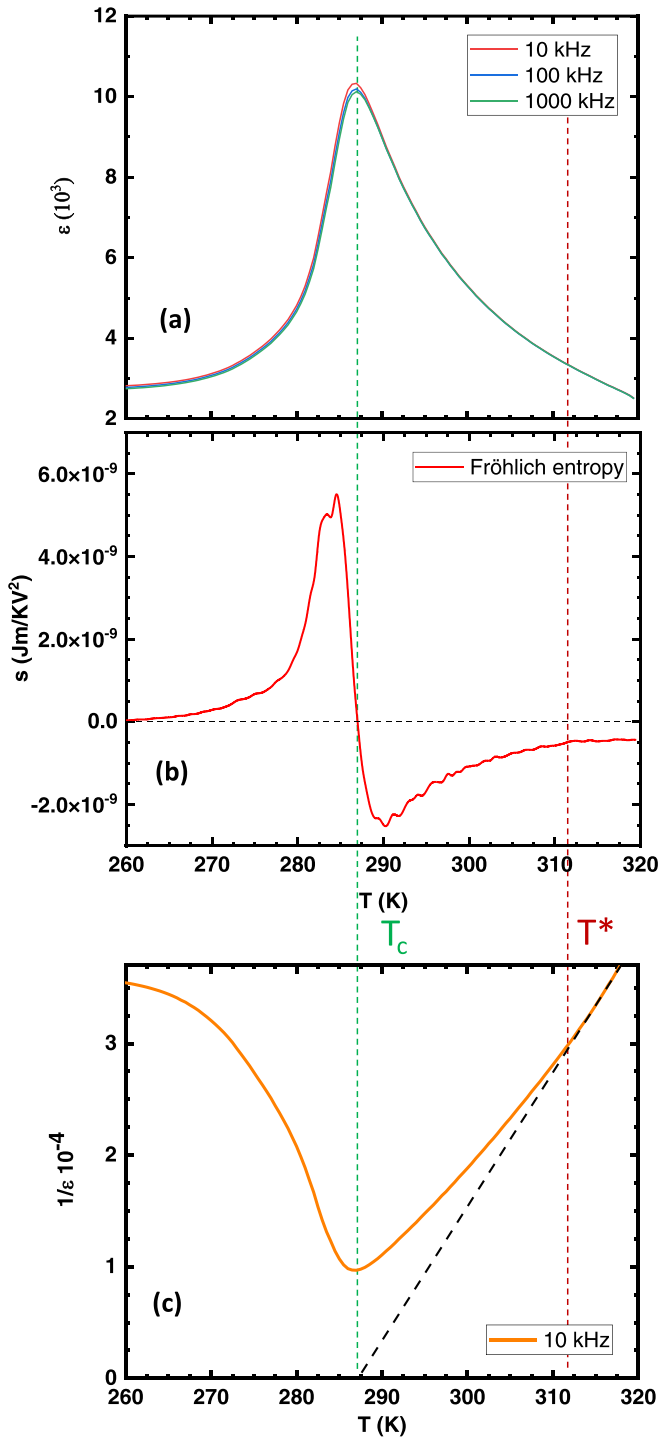


FIG. 1. (a) Dielectric function of the KLTN sample 1 and (b) correlated $s(T)$ Fröhlich entropy, for unit volume and field, as a function of temperature (see text); (c) the inverse of the dielectric function at 10 kHz. $T_{c\text{KLTN1}}$ and T_{KLTN1}^* are also indicated (see text).

symmetry [1,4]. The displayed peak shape is a signature of a diffused relaxor-to-ferroelectric transition (according to the Bokov classification) [1,15]. The curve deviates from the Curie-Weiss law at $T_{\text{KLTN1}}^* \simeq 312$ K, above $T_{c\text{KLTN1}}$ [Fig. 1(c)]. This deviation was attributed to the onset, at T_{KLTN1}^* , of PNRs [1,20,50]. Analogous trends of the relative real permittivity, at

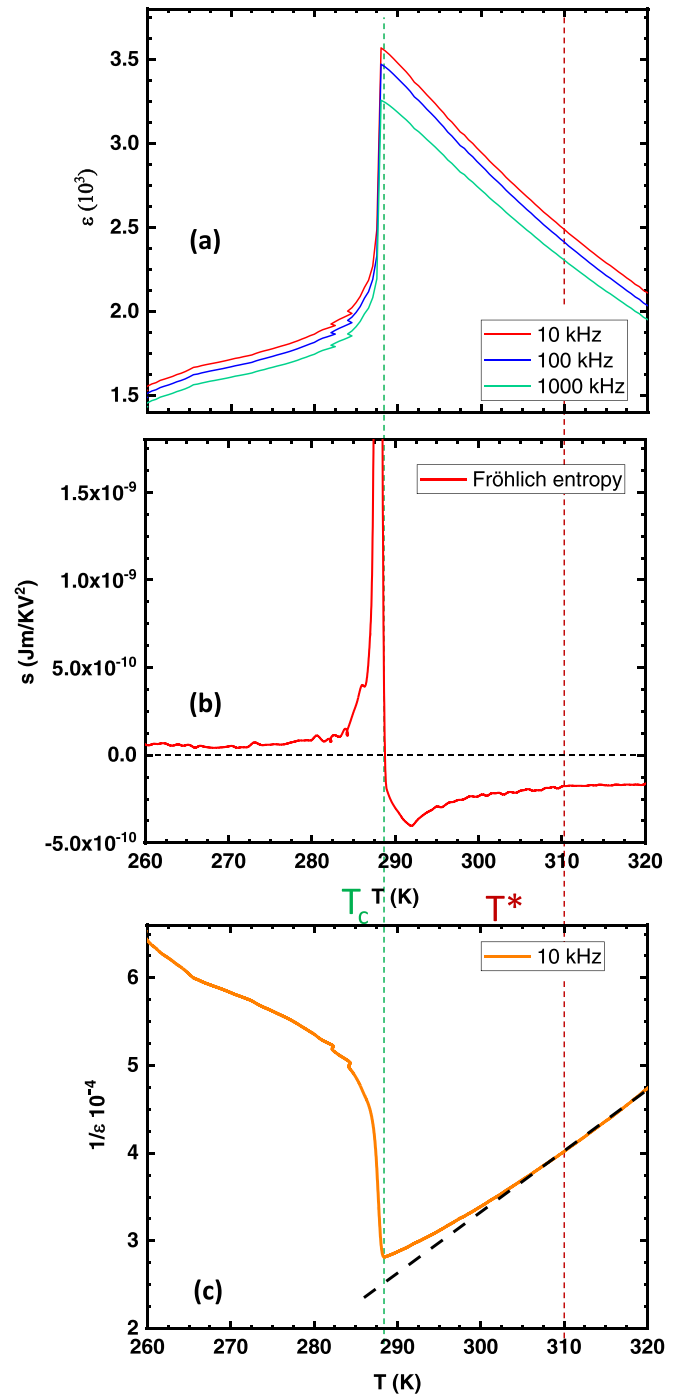


FIG. 2. (a) Dielectric function of the KLTN sample 2 and (b) correlated $s(T)$ Fröhlich entropy, for unit volume and field, as a function of temperature (see text); (c) the inverse of the dielectric function at 10 kHz. $T_{c\text{KLTN2}}$ and T_{KLTN2}^* are also indicated (see text).

the same frequencies and conditions, are shown by Figs. 2(a), 3(a), and 4(a), which are referred to as the KLTN2, KNTN, and KTN samples, respectively. These last ones display peaks analogous to that of the KLTN1 sample, pointing out a slightly diffused relaxor-to-ferroelectric, cubic-to-tetragonal, transition. Similar deviations from Curie-Weiss law are shown by Figs. 3(c) and 4(c) of the corresponding $1/\epsilon(T)$.

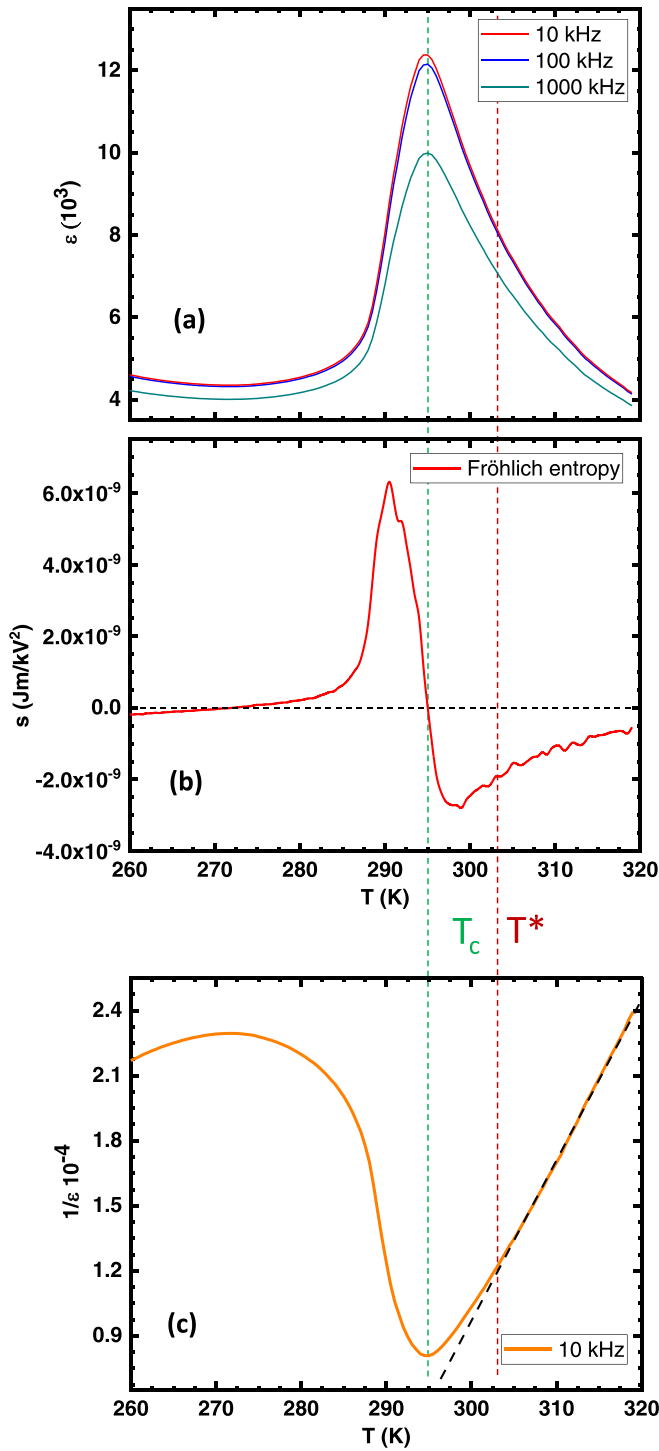


FIG. 3. (a) Dielectric function of the KNTN sample and (b) correlated $s(T)$ Fröhlich entropy, for unit volume and field, as a function of temperature (see text); (c) the inverse of the dielectric function at 10 kHz. T_{cKNTN} and T_{KNTN}^* are also indicated (see text).

Figure 2 refers to the dielectric response of KLTN2, with a different Li content with respect to KLTN1. Figure 2(a) displays its relative real permittivity. Here, the response indicates a very sharp peak ($T_{cKLTN2} \simeq 289$ K), pointing out a canonical ferroelectric behavior [1]: then we associate the inferred T_{cKLTN2} temperature to a sudden tetragonal-to-cubic

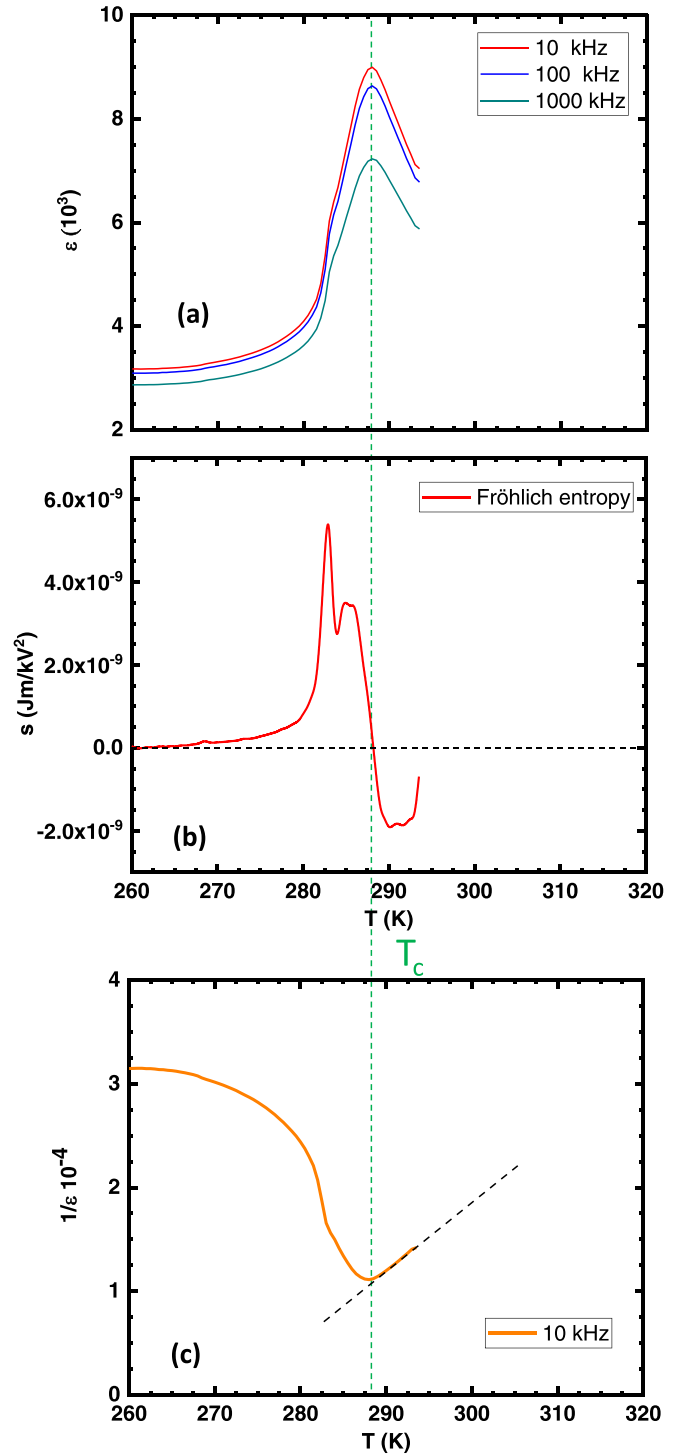


FIG. 4. (a) Dielectric function of the KTN sample and (b) correlated $s(T)$ Fröhlich entropy, for unit volume and field, as a function of temperature (see text); (c) the inverse of the dielectric function at 10 kHz. T_{cKTN} is also indicated (see text).

phase-transition [1,4,5,15]. The plot of $1/\epsilon(T)$ is reported in Fig. 2(c) (for the frequency of 10 kHz). It deviates from the Curie-Weiss law at a T_{KLTN2}^* K, much closer to the T_{cKLTN2} temperature with respect to the case of the KLTN1 sample, as expected in a sample with a sharper transition. The plot in Fig. 2(b) reports the associated Fröhlich entropy. For $T >$

TABLE I. Critical temperatures T_c detected by dielectric measurements for the considered samples. Estimated uncertainty is $\Delta T \simeq 0.25$ K.

Sample	KLTN1	KLTN2	KNTN	KTN
$T_c(K)$	288.5	289	295	287.5

T_{CKLTN2} , $s(T) < 0$ and is almost of constant value, similarly to what happens in KLTN1, KNTN, and KTN.

The temperature dependence of the Fröhlich entropy of KLTN1, KNTN, and KTN crystals, calculated by Eq. (2) at the sample frequency 10 kHz, are reported in Figs. 1(b), 3(b), and 4(b), with similar features. At high temperatures ($T > T^*$), nearly constant negative values of $s(T)$ highlight the inherent polar disorder owing to the chemical compositional disorder with random distribution of Nb^{5+} ions in the B -sublattice and corresponding random electric fields that are largely uncorrelated [50]. Starting below T^* , with the appearance of long-lived reorientable polar nanodomains, the negative curve of $s(T)$ exhibits, upon cooling, a marked decrease. This feature of $s(T)$ reveals the continuous growing of the PNRs' volume fraction with decreasing temperature as above recalled ([9,50,51] and therein). By further lowering the temperature a sudden inversion of the negative trend of $s(T)$ is displayed and, at the critical temperatures given by Table I, abrupt changes of the $s(T)$ sign from negative to positive values occur. These results are the signature of the sharp onset at T_c of different state-of-order in the samples, showing that they undergo disorder/order transitions. Actually, this entropy behavior is in agreement with the randomness dipolar-liquid-like Fröhlich entropy response ($s(T) < 0$) [4,5,13,15,44]. Some irregularities in the shape of the KTN sample entropy curve, such as the two local sharp peaks in Fig. 4(b), are attributed to by inhomogeneities in the chemical substitution, similarly to what was already found in analogous compounds [4,5,31,47]. Above T_c , at the entropy minimum—i.e., 290 K, 298 K, and 290 K for KLTN1, KNTN, and KTN samples, respectively—a sharp disorder-order transition starts centered at T_c . This indicates that polar disorder due to the freely rotating PNRs ceases with a sudden onset of a solid-like dipolar order, as a result of a transition from an uncorrelated to correlated state of the PNRs through a percolative process [9,10,13]. Finally, for $T < T_c$, in the ferroelectric state, $s(T)$ decreases remaining positive.

The very large dielectric permittivity values of such crystals (from $\simeq 10^3$ to $\simeq 10^4$) is a key feature, which the current literature definitely recognized as caused by the giant inherent dipolar moments of PNRs (see, e.g., [1,3,8,9,13,15,20,22,23,50,52]). Due to this unusually large dipolar moments, Fröhlich entropy is almost entirely determined by the behavior of PNRs. Summarizing, in our findings $s(T)$ points out the temperature evolution of the nanodomain system; so our results highlight that the thermal evolution of the PNR system plays a critical role in the occurring of crystalline global transition. These reported experimental data nicely agree with the theoretical discussions and models about the critical role of nanosystems in structural transitions by Goodwin *et al.* and by Xu *et al.* [16,17,52].

IV. RAMAN RESPONSE

Temperature-resolved Raman responses are reported in Fig. 5 for KLTN1 [Fig. 5(a)] and KLTN2 [Fig. 5(b)] and in Fig. 6 for KNTN [Fig. 6(a)] and KTN [Fig. 6(b)] samples, where intensity-reduced spectra are calculated from Eq. (3). Since first-order Raman scattering is absent for cubic symmetry, we attribute the observed Raman response in all samples to local symmetry breaking, a phenomenon typical of systems that manifest local polarized mesoscopic domains [32,35,36,39].

First we analyze the features of the so-called $TO4$ peak, which are shown as a function of the temperature in Figs. 7–10 for KLTN1, KLTN2, KNTN, and KTN, respectively. This Raman peak, displaying features of a *soft mode*, is identified in agreement with similar perovskitic crystals [19,53–56]. Notably, the behavior of this Raman mode is correlated to local polarized regions that display relaxation [19]. Namely, the temperature evolution of reduced intensity of the peak height $H_{TO4}(T)$ is depicted in Figs. 7(a), 8(a), 9(a), and 10(a).

In KLTN1 we note that, upon cooling, H_{TO4} shows a first temperature region (from 322 K to 312 K) where a slight increase is found. A sharp deviation in the temperature evolution of the considered mode is observed at $T \simeq T_{\text{CKLTN1}}^*$ (312 K), i.e., for the temperature at which the dielectric response suggests the onset of permanent PNRs [Fig. 1(c)]. After a plateau, the height of the $TO4$ decreases until $T = T_{\text{CKLTN1}}$ ($\simeq 288$ K). Thereafter, between T_{CKLTN1} and T_{fKLTN1} , a decrease is found. Finally, at $T = T_{\text{fKLTN1}}$ $H_{TO4}(T)$ starts to increase again. We note that, from high to low temperatures, the respective peak width has a slightly increasing trend up to 288 K ($\simeq T_{\text{CKLTN1}}$), while its width strongly decreases below T_{CKLTN1} [Fig. 7(b)]. This observed evolution of $TO4$ in KLTN1 confirms the occurring of a phase-transition at $T = T_{\text{CKLTN1}}$ [19,32,39]. The ever-slower decrease of $H_{TO4}(T)$ between T_{CKLTN1} and T_{fKLTN1} is compatible with the features of the diffuse transition typical of relaxors [1,4,19]. Hence the temperature T_{fKLTN1} marks the end of the phase-transition. If we compare Raman behavior to the dielectric response we will find a marked correspondence between the previously identified temperature regions. In particular, the region between T_{fKLTN1} and T_{CKLTN1} , where both H_{TO4} and the peak width w_{TO4} are almost constant, indicate the temperature interval of the pretransitional phenomena, while the interval between T_{CKLTN1}^* and T_{fKLTN1} delimits the region where the entire transition occurs.

In KLTN2 the $TO4$ mode, on the other hand, displays different features (Fig. 8). Here, the trend of H_{TO4} as a function of T can be divided in two ranges only. The first temperature region (from 315 K to 289 K), where a the trend is slightly constant, and a second region below T_{CKLTN2} ($\simeq 289$ K) where H_{A1g} constantly decreases. Finally, at $T = T_{\text{fKLTN2}}$ ($\simeq 273$ K) $H_{TO4}(T)$ starts to increase again. It is worth noting that the sharpness of the transition highlighted by the dielectric response (Fig. 2) is here reproduced in the behavior of the $TO4$ Raman-mode temperature evolution.

The $TO4$ peak in KNTN and KTN samples (Figs. 9 and 10) displays a growing of H_{TO4} upon cooling, until a temperature $T = T_{\text{CKNTN}}^* = T_{\text{CKTN}}^* \simeq 294$ K. Then, a temperature region can be found between T^* and T_c . For the KNTN sample there is a very sharp peak, both in the plots of H_{TO4} and w_{TO4} [Figs. 9(a)

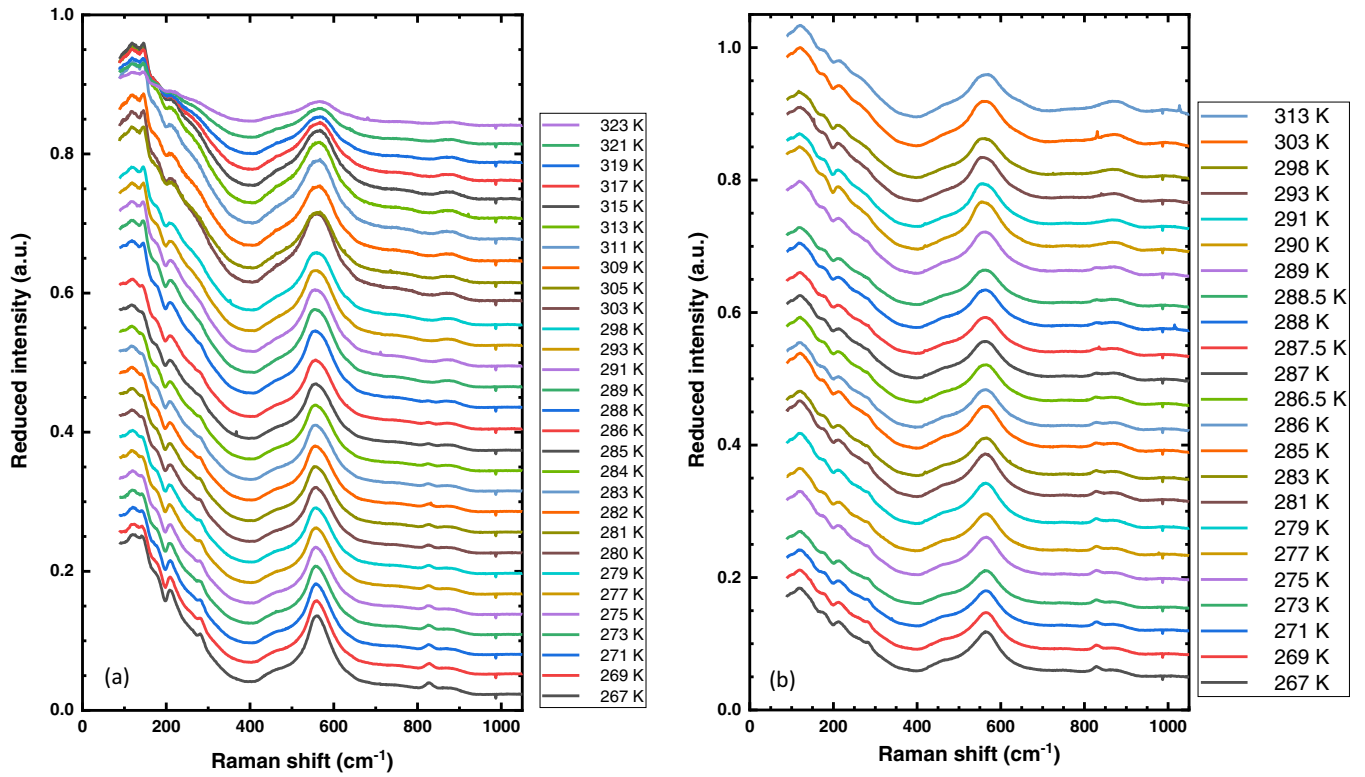


FIG. 5. Landscape of the reduced intensity of Raman spectra measured on the KLTN (a) sample 1 and (b) sample 2.

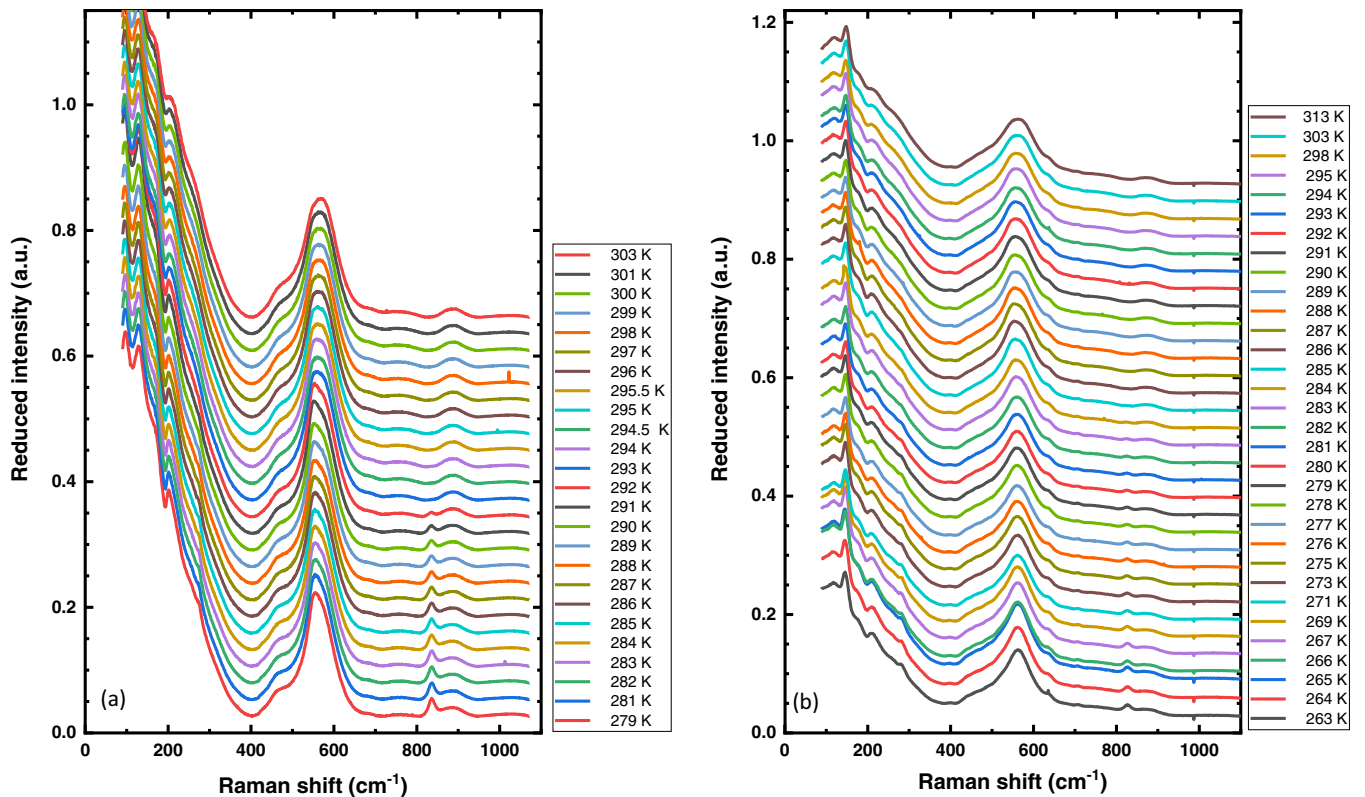


FIG. 6. Landscape of the reduced intensity of Raman spectra measured on the (a) KNTN and (b) KTN samples.

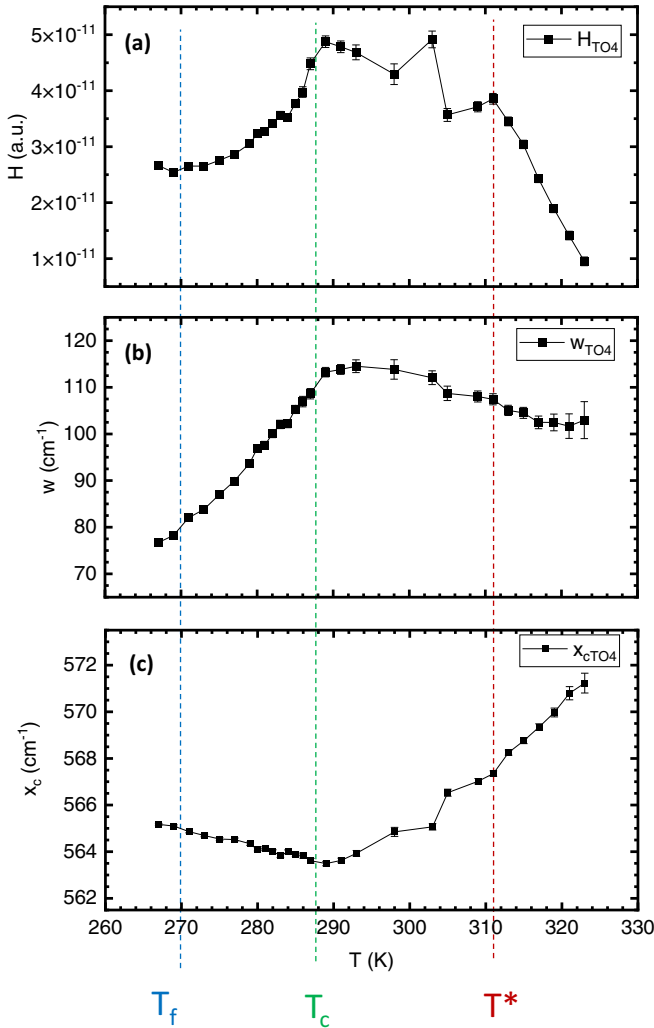


FIG. 7. Trend of the reduced intensity of the $TO4$ peak obtained from the global Raman spectra as a function of temperature of KLTN1: (a) height [$H_{TO4} = H_{TO4}(T)$]; (b) width [$w_{TO4} = w_{TO4}(T)$]; and (c) center of the peak [$x_c = x_c(T)$] as obtained by Lorentzian fits. The three characteristic detected critical temperatures, T_{fKLTN1} , T_{cKLTN1} , and T_{KLTN1}^* , are also indicated (see text).

and 9(b)], while for KTN sample the trend has a plateau-step shape for both the H_{TO4} and w_{TO4} parameters [Figs. 10(a) and 10(b)]. Below T_c an evident decrease of H_{TO4} marks the phase transition highlighted by the dielectric responses (Figs. 3 and 4) in both samples; the inspected decrease is much faster for KNTN than for KTN.

In Figs. 11 and 12 the Raman spectra are evidenced in the range $650\text{--}950\text{ cm}^{-1}$ for selected temperatures. The sudden arising of a new mode around 830 cm^{-1} is detected when the temperature is lowered to about $T = 288\text{ K}$ (for KLTN1 and KTN), $T = 289\text{ K}$ (for KLTN2), and $T = 295\text{ K}$ (for KNTN). The appearance of this mode, which we call the “*transition mode*,” is in strict correspondence with the T_c temperatures (Table I), which were above pointed out by dielectric analysis. Specifically, we note that, for each sample, the temperature where this mode arises corresponds to the center of the sharp order-disorder transition which is highlighted by Fröhlich entropy behavior, as depicted by Figs. 1(b), 2(b), 3(b), and 4(b).

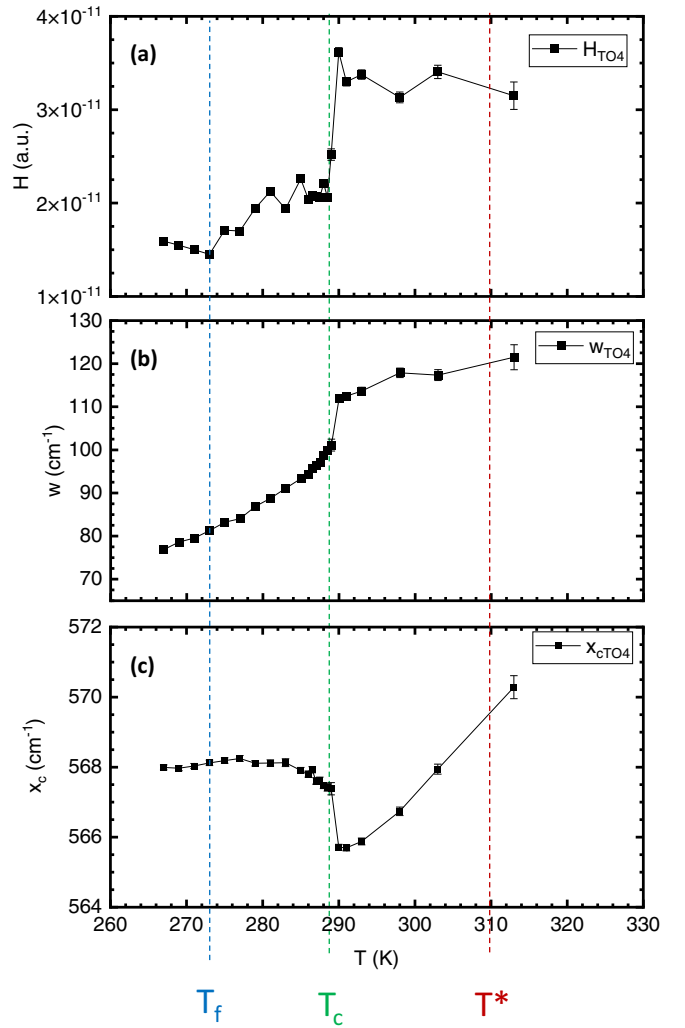


FIG. 8. Trend of the reduced intensity of the $TO4$ peak obtained from the global Raman spectra as a function of temperature of KLTN2: (a) height [$H_{TO4} = H_{TO4}(T)$]; (b) width [$w_{TO4} = w_{TO4}(T)$]; and (c) center of the peak [$x_c = x_c(T)$] as obtained by Lorentzian fits. The three characteristic detected critical temperatures, T_{fKLTN2} , T_{cKLTN2} , and T_{KLTN2}^* , are also indicated (see text).

We here stress the discontinuous appearance of this *transition mode*: above T_c (referred to all samples) no signals of its presence can be detected, below T_c it abruptly arises (Figs. 11 and 12). Fröhlich entropy behavior and the sudden appearance of the $s(T)$ peak indicate that this mode is caused by a percolative mechanism establishing a robust ordering, which we associate to the evolution of the PNR system. The features of the considered Raman mode as a function of the temperature, whose parameters are obtained through suitable Lorentzian fits, are reported in Figs. 13–16.

Lowering the temperature, after the sudden arise of this mode, at T_c , the height H of the peak linearly increases for all samples [Figs. 13(a), 14(a), 15(a), and 16(a)]. Similarly, the center of this Raman peak increases almost linearly for KLTN1, KLTN2, and KTN samples [Figs. 13(c), 14(c), and 16(c)], while it remains unchanged for the KNTN crystal [Fig. 15(c)]. For the first three samples, in the considered temperature region, $x_c(T)$ passes from about $x_c = 826.9\text{ cm}^{-1}$

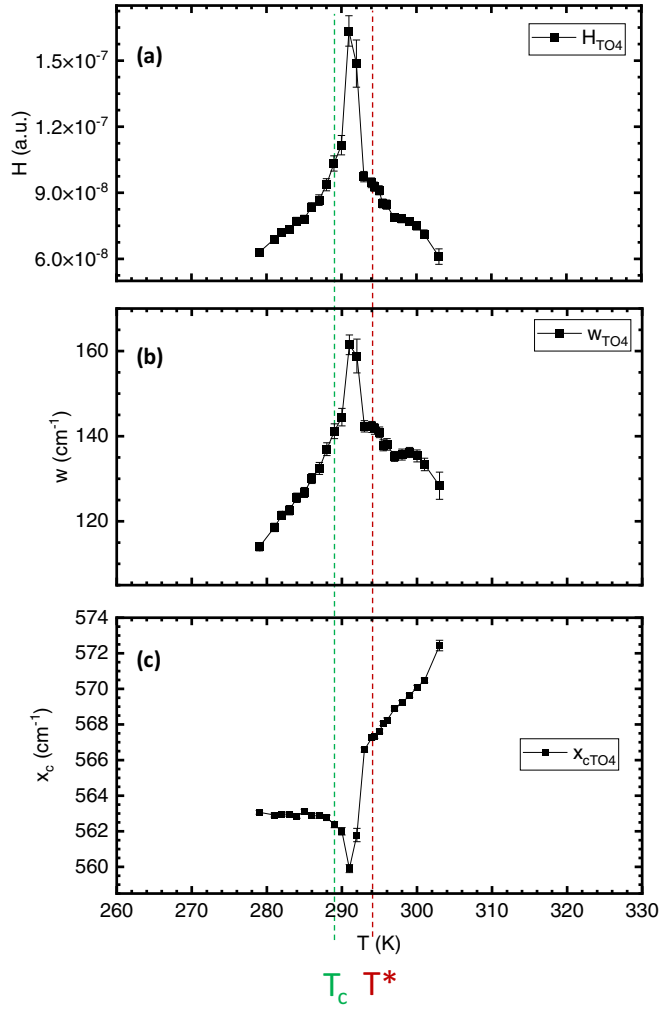


FIG. 9. Trend of the reduced intensity of the $TO4$ peak obtained from the global Raman spectra as a function of temperature of KNTN: (a) height [$H_{TO4} = H_{TO4}(T)$]; (b) width [$w_{TO4} = w_{TO4}(T)$]; and (c) center of the peak [$x_c = x_c(T)$] as obtained by Lorentzian fits. The characteristic detected critical temperatures T_{cKNTN} and T_{KNTN}^* are also indicated (see text).

at $T = 288$ K, to $x_c \simeq 828.2$ cm^{-1} at $T = 266$ K for KLTN1 and $x_c \simeq 827.3$ cm^{-1} at $T = 289$ K, to $x_c \simeq 828.3$ cm^{-1} at $T = 266$ K for KLTN2, and from about $x_c \simeq 826.3$ cm^{-1} at $T = 285$ K, to $x_c \simeq 827.6$ cm^{-1} at $T = 263$ K for KTN; for KNTN it remains at $x_c \simeq 835$ cm^{-1} . On the other hand, the peak width remains approximately constant [Figs. 13(b), 14(b), 15(b), and 16(b)] for all the samples; we note that KLTN1, which is more disordered, has a larger width (23 cm^{-1} on average) than KLTN2 (20 cm^{-1} on average).

Our interpretation of this inspected Raman mode is based on the temperature evolution of PNRs provided by the Fröhlich entropy [44]. The negative value of $s(T)$ above T_c , in all the considered samples, is attributed, as previously discussed, to the dielectric response of uncorrelated PNRs, which display a polar liquid-like behavior [5]. The sign change of the Fröhlich entropy signals the loss of orientational freedom, with the transition to a correlated state, accordingly to a polar solid-like positive $s(T)$ response [5,46]. In simple terms, the

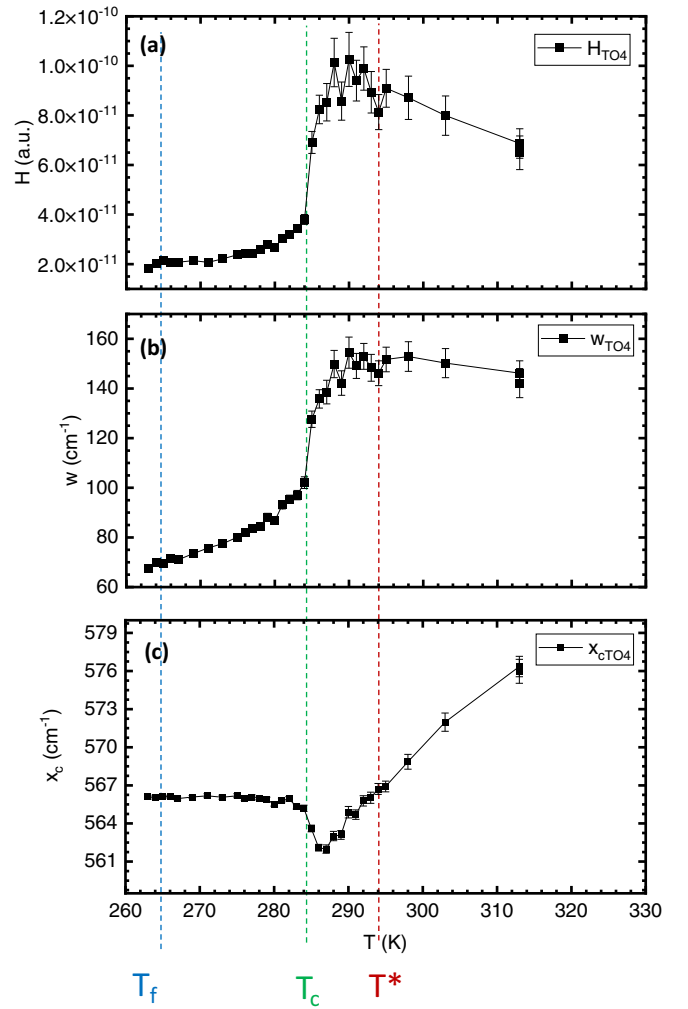


FIG. 10. Trend of the reduced intensity of the $TO4$ peak obtained from the global Raman spectra as a function of temperature of KNTN: (a) height [$H_{TO4} = H_{TO4}(T)$]; (b) width [$w_{TO4} = w_{TO4}(T)$]; and (c) center of the peak [$x_c = x_c(T)$] as obtained by Lorentzian fits. The three characteristic detected critical temperatures, T_{fKNTN} , T_{cKNTN} , and T_{KNTN}^* are also indicated (see text).

disorder-order transition corresponds to the transition from an uncorrelated to a correlated state of the PNRs. The Raman *transition mode* is associated to the onset of this correlation. Fröhlich entropy indicates that this onset is correlated with the rise of a new PNR arrangement. Hence, the fact that the mode suddenly appears at T_c , with an evident discontinuity, highlights that it is correlated with a temperature-activated percolative process, in agreement with the analogous behaviors pointed out in similar perovskites [10–13,40,52]. After the percolation temperature threshold of T_c , the strictly interacting (ordered) PNRs are able to produce a collective response, which is highlighted by the *transition mode*.

V. CONCLUSION

We investigated the dielectric response and Raman experiments in different compositionally disordered potassium-based perovskite single crystals as a function of temperature.

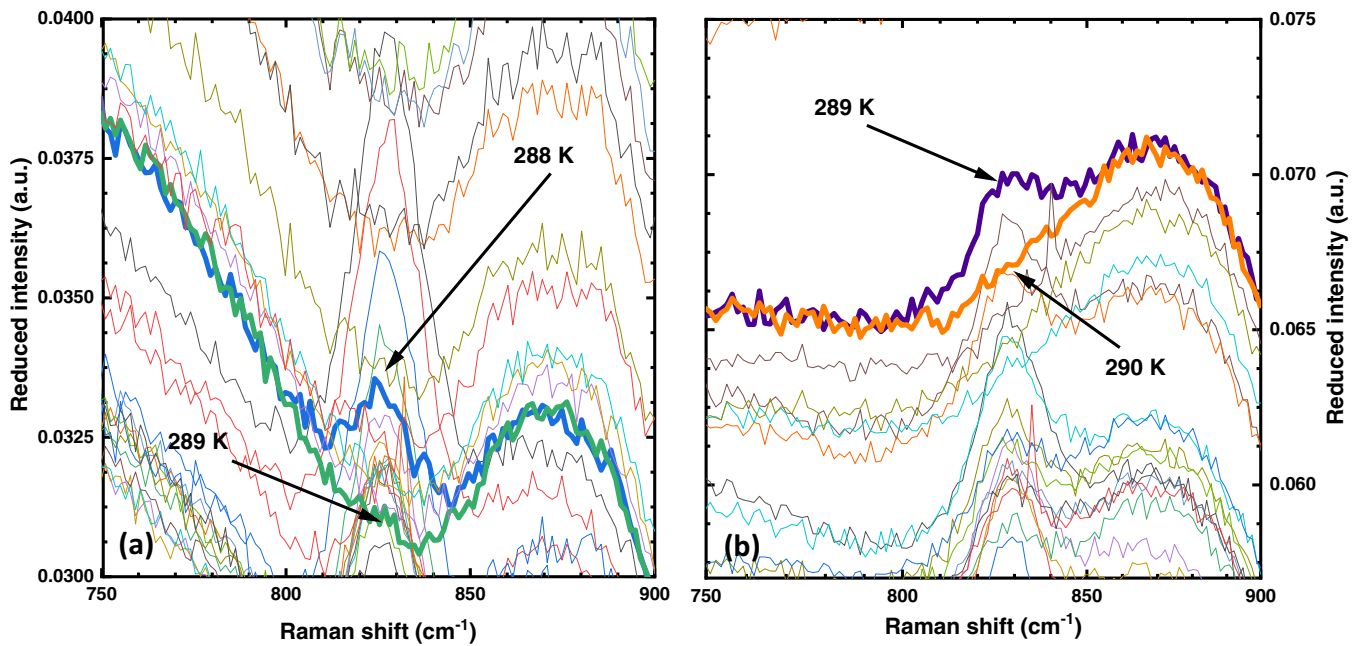


FIG. 11. Zoom of Raman spectra of Fig. 5 at selected temperatures for (a) KLTN1 and (b) KLTN2: the abrupt arising of the Raman modes around 827 cm^{-1} is evidenced.

The results are correlated to each other through the evaluation of Fröhlich entropy. The analysis of the spectral peaks is focused on two specific Raman modes. The first one is the so-called TO_4 peak, whose features have been demonstrated to finely display the temperature evolution of the cubic-to-tetragonal long-range phase transition. The second considered peak of the Raman spectrum, centered around 830 cm^{-1} , is a Raman mode (*transition mode*) which was never previously discussed and analyzed. Comparison to dielectric measurements allows us to associate this mode to the change of the

order state of PNRs, so its arising temperature as the signature of an effective cubic-to-tetragonal phase transition.

We stress that, due to the recalled giant dipole moment of PNRs, the dielectric response and Fröhlich entropy give information belonging to the mesoscopic realm. Congruently, our findings give the evidence that the PNRs order-disorder (correlated-uncorrelated) transition, i.e., the mesoscopic rearrangement, turns on the global phase transition. Although providing a comprehensive theoretical picture correlating microscopic/mesoscopic features of ferroelectrics with

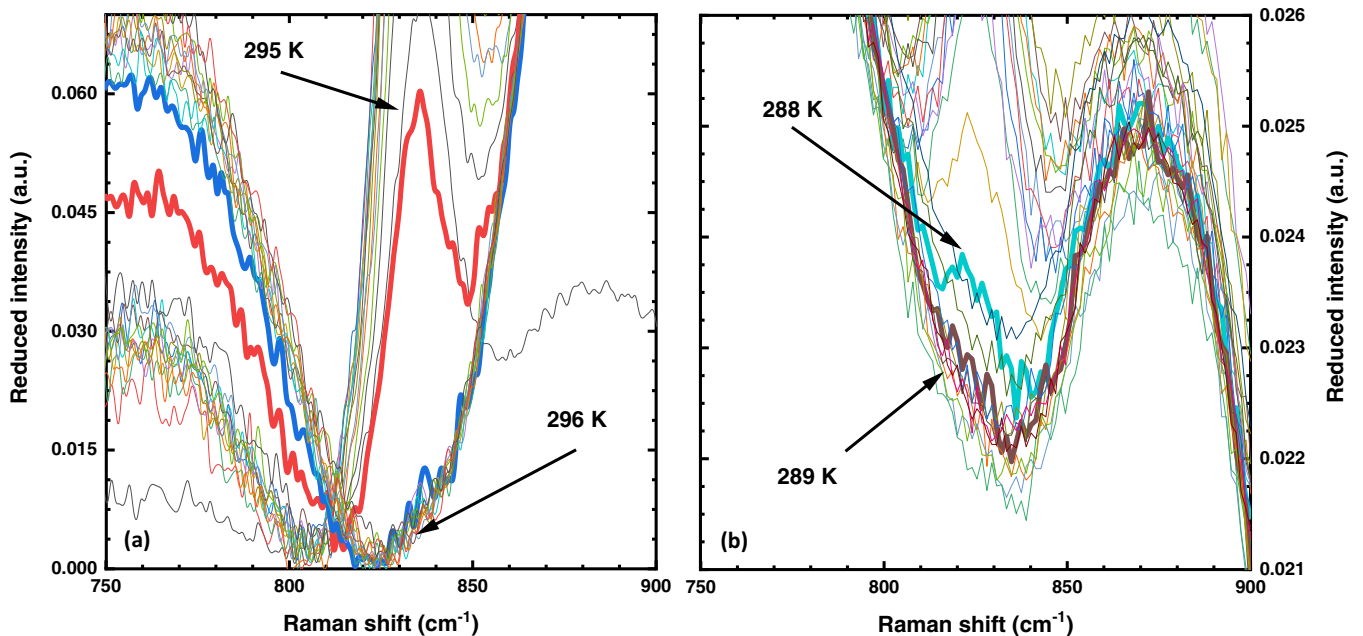


FIG. 12. Zoom of Raman spectra of Fig. 6 at selected temperatures for (a) KNTN and (b) KTN: the abrupt arising of the Raman modes around 835.7 and 821.3 cm^{-1} (respectively) is evidenced.

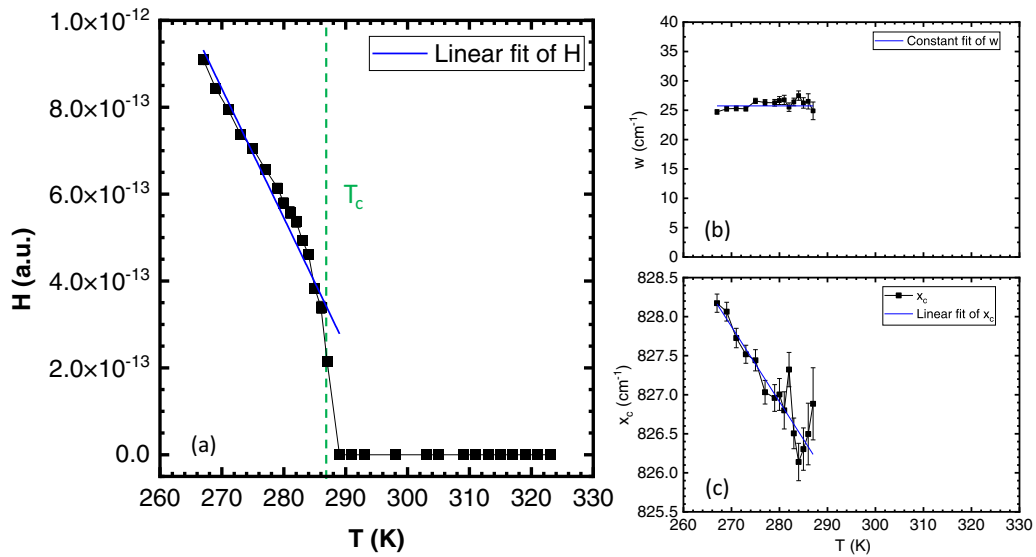


FIG. 13. Trend of the 827 cm^{-1} transition mode as a function of temperature in KLTN1: (a) height [$H_{\text{mode}} = H_{\text{mode}}(T)$]; (b) width [$w_{\text{mode}} = w_{\text{mode}}(T)$]; and (c) peak position [$x_c = x_c(T)$] as obtained by Lorentzian fits. The characteristic detected critical temperature of the mode insurgence T_{C1} is evidenced.

macroscopic behavior is a still open investigation issue, we underline that our experimental results are in agreement with recently developed models [16,17,52].

For all the investigated samples, we can summarize our findings in the following main items.

(1) Dielectric and Raman findings show a structural transition at T_c .

(2) The structural crystalline transformation corresponds to an ordering process of the PNRs from an uncorrelated to a correlated state that happens at T_c . Namely, PNRs above T_c are randomly oriented (disordered), below T_c they are in

a ferroelectric state. This result highlights the critical role of the mesoscopic polar systems in the occurrence of the global crystalline transition.

(3) A strong order-disorder component is assessed in the investigated transition.

(4) At this same T_c temperature the abrupt arising of a new Raman mode demonstrates a percolative character of the PNRs cooperative order establishing.

(5) The sudden onset at T_c of this new Raman mode is found, which we call the *transition mode*, centered at about 830 cm^{-1} (i.e., the onset in the sample of a new structure).

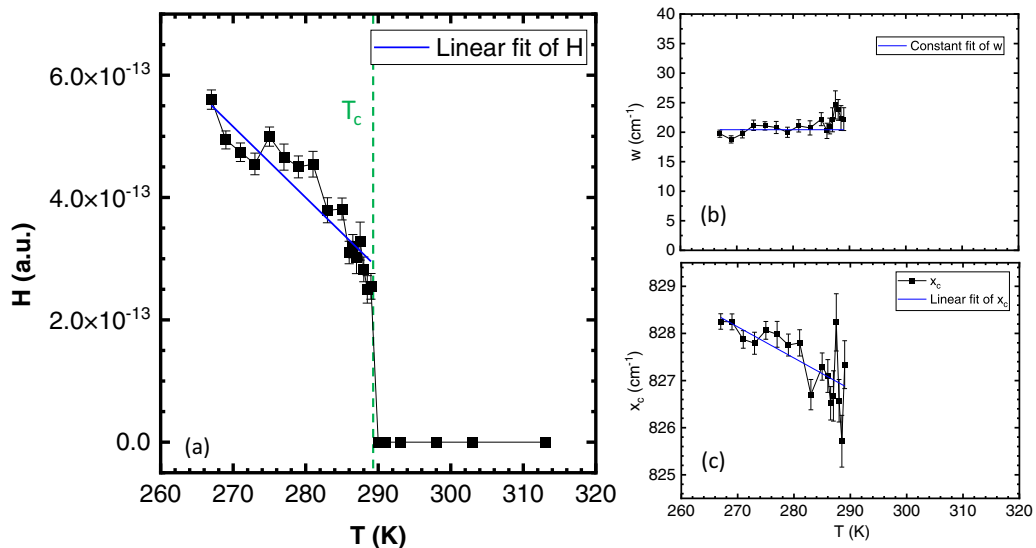


FIG. 14. Trend of the 827 cm^{-1} transition mode as a function of temperature in KLTN2: (a) height [$H_{\text{mode}} = H_{\text{mode}}(T)$]; (b) width [$w_{\text{mode}} = w_{\text{mode}}(T)$]; and (c) peak position [$x_c = x_c(T)$] as obtained by Lorentzian fits. The characteristic detected critical temperature of the mode insurgence T_{C2} is evidenced.

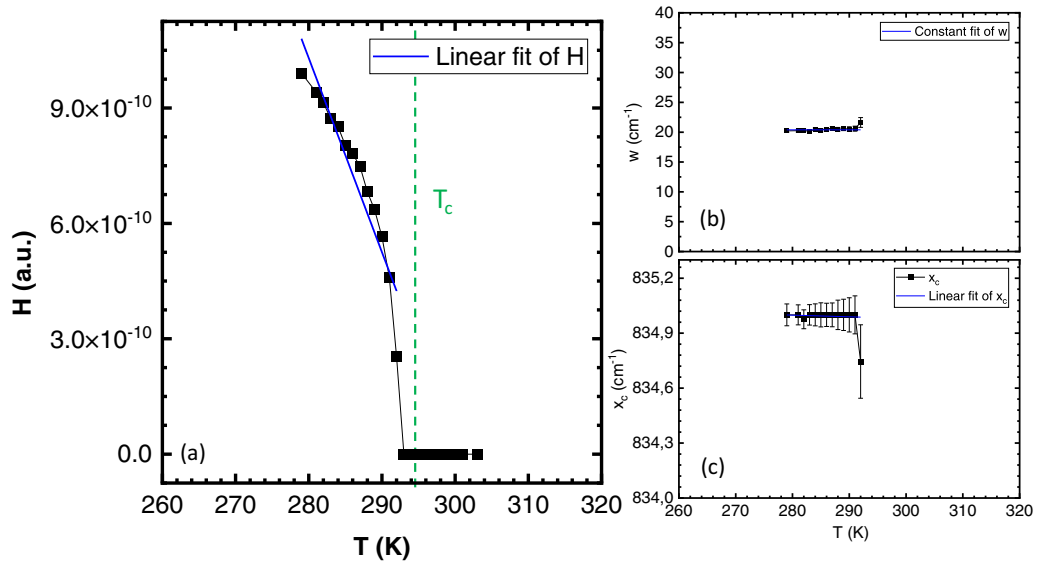


FIG. 15. Trend of the *transition mode*, here at 835 cm^{-1} , as a function of temperature in KNTN: (a) height [$H_{\text{mode}} = H_{\text{mode}}(T)$]; (b) width [$w_{\text{mode}} = w_{\text{mode}}(T)$]; and (c) peak position [$x_c = x_c(T)$] as obtained by Lorentzian fits. The characteristic detected critical temperature of the mode insurgence T_{C3} is evidenced.

(6) Both Fröhlich entropy behavior and Raman response demonstrate that the cubic-to-tetragonal transition displays the feature of a percolative phenomenon.

(7) Results appear to have a general validity, at least for potassium-based oxide perovskite single-crystals.

This behavior is found in all the four inspected samples: two different KLTN with a diffused and a sharp ferroelectric transition, KNTN, and KTN. An open issue is the development of a theoretical model describing the pointed out Raman mode evolution, which will be the subject of future works. The here reported results allow us to establish a critical temperature, signaling the long-range symmetry transformation,

independently of its diffused or sharp character. This supports the idea that the formation of mesoscopic structures is able to create a specific phononic frequency, making Raman spectroscopy a suitable tool for inspecting the behavior of such systems. Furthermore, the inspected temperature of mode activation can be assumed as the temperature where the phase transition occurs.

ACKNOWLEDGMENT

J.P. and GB.P. thank M. Moscardini for technical assistance in dielectric measurements.

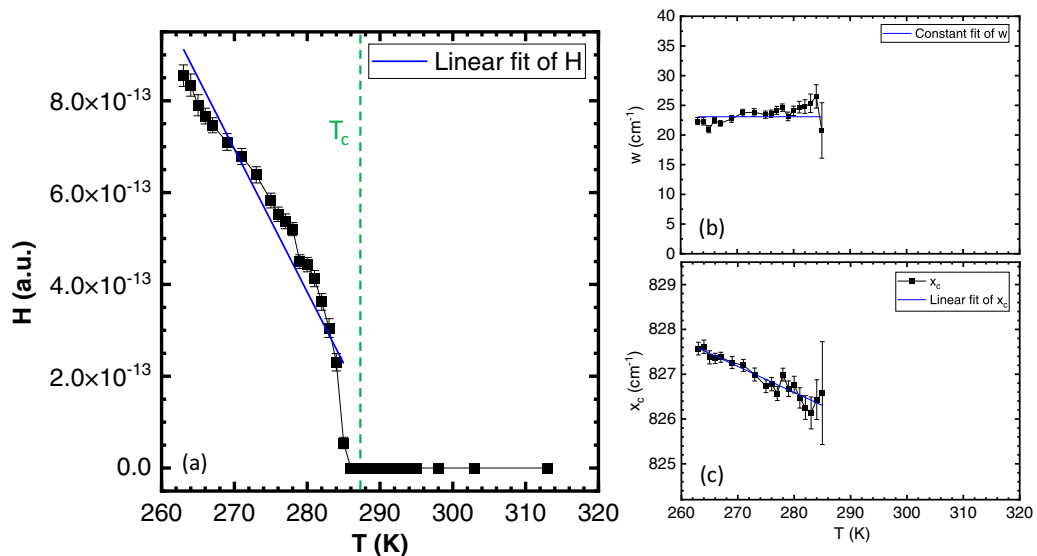


FIG. 16. Trend of the 827 cm^{-1} *transition mode* as a function of temperature in KTN: (a) height [$H_{\text{mode}} = H_{\text{mode}}(T)$]; (b) width [$w_{\text{mode}} = w_{\text{mode}}(T)$]; and (c) peak position [$x_c = x_c(T)$] as obtained by Lorentzian fits.

- [1] A. Bokov, Recent progress in relaxor ferroelectrics with perovskite structure, *J. Mater. Sci.* **41**, 31 (2006).
- [2] E. DelRe, E. Spinozzi, A. J. Agranat, and C. Conti, Scale-free optics and diffractionless waves in nanodisordered ferroelectrics, *Nat. Photonics* **5**, 39 (2011).
- [3] E. DelRe, F. D. Mei, J. Parravicini, G. Parravicini, A. Agranat, and C. Conti, Subwavelength anti-diffracting beams propagating for more than 1,000 rayleigh lengths, *Nat. Photonics* **9**, 228 (2015).
- [4] J. Parravicini, E. DelRe, A. J. Agranat, and G. B. Parravicini, Macroscopic response and directional disorder dynamics in chemically substituted ferroelectrics, *Phys. Rev. B* **93**, 094203 (2016).
- [5] J. Parravicini, E. DelRe, A. J. Agranat, and G. B. Parravicini, Liquid-solid directional composites and anisotropic dipolar phases of polar nanoregions in disordered perovskite, *Nanoscale* **9**, 9572 (2017).
- [6] F. D. Mei, L. Falsi, M. Flammini, D. Pierangeli, P. D. Porto, A. J. Agranat, and E. DelRe, Giant broadband refraction in the visible in a ferroelectric perovskite, *Nat. Photonics* **12**, 734 (2018).
- [7] N. Balke, S. Choudhury, S. Jesse, M. Huijben, Y. Chu, A. Baddorf, L. Chen, R. Ramesh, and S. V. Kalinin, Deterministic control of ferroelastic switching in multiferroic materials, *Nat. Nanotechnol.* **4**, 868 (2009).
- [8] J. Toulouse, D. La-Orautapong, and O. Svitelskiy, Dynamics of polar nanoregions in relaxors, *Ferroelectrics* **302**, 271 (2004).
- [9] D. Fu, H. Taniguchi, M. Itoh, and S. Mori, Pb(Mg_{1/3}Nb_{2/3})O₃ (PMN) Relaxor: Dipole glass or nano-domain ferroelectric? in *Advances in Ferroelectrics* (IntechOpen, London, 2012), Chap. 3, pp. 51–67.
- [10] S. Prosandeev, D. Wang, A. R. Akbarzadeh, B. Dkhil, and L. Bellaiche, Field-Induced Percolation of Polar Nanoregions in Relaxor Ferroelectrics, *Phys. Rev. Lett.* **110**, 207601 (2013).
- [11] U. Bianchi, W. Kleemann, and J. Bednorz, Raman scattering of ferroelectric Sr_{1-x}Ca_xTiO₃, $x = 0.007$, *J. Phys.: Condens. Matter* **6**, 1229 (1994).
- [12] S. Lerner, P. B. Ishai, A. Agranat, and Y. Feldman, Percolation of polar nanoregions: A dynamic approach to the ferroelectric phase transition, *J. Non-Cryst. Solids* **353**, 4422 (2007).
- [13] R. Pirc and Z. Kutnjak, Freezing in relaxor ferroelectrics and dipolar glasses, *Phase Transitions* **88**, 222 (2015).
- [14] S. Prosandeev, D. Wang, A. R. Akbarzadeh, and L. Bellaiche, First-principles-based effective hamiltonian simulations of bulks and films made of lead-free Ba(Zr, Ti)O₃ relaxor ferroelectrics, *J. Phys.: Condens. Matter* **27**, 223202 (2015).
- [15] P. Tan, H. Tian, C. Mao, C. Hu, X. Meng, L. Li, G. Shi, and Z. Zhou, Field-driven electro-optic dynamics of polar nanoregions in nanodisordered KTa_{1-x}Nb_xO₃ crystal, *Appl. Phys. Lett.* **111**, 012903 (2017).
- [16] M. S. Senn, D. A. Keen, T. C. A. Lucas, J. A. Hriljac, and A. L. Goodwin, Emergence of Long-Range Order in BaTiO₃ from Local Symmetry-Breaking Distortions, *Phys. Rev. Lett.* **116**, 207602 (2016).
- [17] D. A. Keen and A. L. Goodwin, The crystallography of correlated disorder, *Nature (London)* **521**, 303 (2015).
- [18] G. Burns and F. Dacol, Glassy polarization behavior in ferroelectric compounds Pb(Mg_{1/3}Nb_{2/3})O₃ and Pb(Zn_{1/3}Nb_{2/3})O₃, *Solid State Commun.* **48**, 853 (1983).
- [19] J. Toulouse, F. Jiang, O. Svitelskiy, W. Chen, and Z.-G. Ye, Temperature evolution of the relaxor dynamics in Pb(Zn_{1/3}Nb_{2/3})O₃: A critical Raman analysis, *Phys. Rev. B* **72**, 184106 (2005).
- [20] J. Toulouse, The three characteristic temperatures of relaxor dynamics and their meaning, *Ferroelectrics* **369**, 203 (2008).
- [21] A. Agranat, R. Hofmeister, and A. Yariv, Characterization of a new photorefractive material: K_{1-y}Li_yTa_{1-x}N_x, *Opt. Lett.* **17**, 713 (1992).
- [22] Y. Chang, C. Wang, S. Yin, R. Hoffman, and A. Mott, Kovacs effect enhanced broadband large field of view electro-optic modulators in nanodisordered KTN crystals, *Opt. Express* **21**, 17760 (2013).
- [23] Y. Chang, C. Wang, S. Yin, R. Hoffman, and A. Mott, Giant electro-optic effect in nanodisordered KTN crystals, *Opt. Lett.* **38**, 4574 (2013).
- [24] J. Parravicini, F. Di Mei, C. Conti, A. Agranat, and E. DelRe, Diffraction cancellation over multiple wavelengths in photorefractive dipolar glasses, *Opt. Express* **19**, 24109 (2011).
- [25] D. Pierangeli, M. Flammini, F. Di Mei, J. Parravicini, C. E. M. deOliverira, A. J. Agranat, and E. DelRe, Continuous Solitons in a Lattice Nonlinearity, *Phys. Rev. Lett.* **114**, 203901 (2015).
- [26] J. Parravicini, A. Agranat, C. Conti, and E. DelRe, Equalizing disordered ferroelectrics for diffraction cancellation, *Appl. Phys. Lett.* **101**, 111104 (2012).
- [27] J. Parravicini, C. Conti, A. Agranat, and E. DelRe, Programming scale-free optics in disordered ferroelectrics, *Opt. Lett.* **37**, 2355 (2012).
- [28] J. Parravicini, D. Pierangeli, F. Di Mei, C. Conti, A. Agranat, and E. DelRe, Aging solitons in photorefractive dipolar glasses, *Opt. Express* **21**, 30573 (2013).
- [29] J. Parravicini, A. Agranat, C. Conti, and E. DelRe, Rejuvenation in scale-free optics and enhanced diffraction cancellation lifetime, *Opt. Express* **20**, 27382 (2012).
- [30] L. Falsi, L. Tartara, F. Di Mei, M. Flammini, J. Parravicini, D. Pierangeli, G. Parravicini, X. Feifei, P. DiPorto, A. Agranat, and E. DelRe, Constraint-free wavelength conversion supported by giant optical refraction in a 3d perovskite supercrystal, *Commun. Mater.* **1**, 76 (2020).
- [31] L. Lo Presti, J. Parravicini, R. Soave, G. Parravicini, M. Mauri, L. Loconte, F. Di Mei, L. Falsi, L. Tartara, S. Binetti, A. J. Agranat, and E. DelRe, Observation of an exotic lattice structure in the transparent KTa_{1-x}Nb_xO₃ perovskite supercrystal, *Phys. Rev. B* **102**, 214110 (2020).
- [32] M. Rahaman, T. Imai, T. Sakamoto, S. Tsukada, and S. Kojima, The role of polar-nanoregions in Li-doped KTa_{1-x}Nb_xO₃ single crystals studied by Raman scattering, *Ferroelectrics* **503**, 85 (2016).
- [33] M. Rahaman, T. Imai, T. Sakamoto, M. A. Helal, S. Tsukada, and S. Kojima, Ferroelectric phase transition of Li-doped KTa_{1-x}Nb_xO₃ single crystals with weak random fields: Inelastic light scattering study, *J. Alloys Compd.* **735**, 1063 (2018).
- [34] L. Cai, R. Pattnaik, J. Lundeen, and J. Toulouse, Piezoelectric polar nanoregions and relaxation-coupled resonances in relaxor ferroelectrics, *Phys. Rev. B* **98**, 134113 (2018).
- [35] V. A. Trepakov, M. E. Savinov, E. Giulotto, P. Galinetto, P. Camagni, G. Samoggia, L. A. Boatner, and S. E. Kapphan, Dipole ordering effects and reentrant dipolar

- glass state in $\text{KTaO}_3\text{:Li,Nb}$, *Phys. Rev. B* **63**, 172203 (2001).
- [36] P. Galinetto, E. Giulotto, G. Samoggia, V. A. Trepakov, S. E. Kapphan, L. Jastrabik, and L. A. Boatner, Study of dipole ordering in $\text{K}_{1-x}\text{Li}_x\text{Ta}_{1-y}\text{Nb}_y\text{O}_3$ by Raman spectroscopy, *Jpn. J. Appl. Phys.* **41**, 7181 (2002).
- [37] S. Kojima, M. M. Rahaman, R. Sase, T. Hoshina, and T. Tsurumi, Vibrational dynamics of ferroelectric $\text{K}(\text{Ta}_{1-x}\text{Nb}_x)\text{O}_3$ studied by far-infrared spectroscopic ellipsometry and Raman scattering, *Jpn. J. Appl. Phys.* **57**, 11UB05 (2018).
- [38] O. Svitelskiy, J. Toulouse, G. Yong, and Z. G. Ye, Polarized Raman study of the phonon dynamics in $\text{Pb}(\text{Mg}_{1/3}\text{Nb}_{2/3})\text{O}_3$ crystal, *Phys. Rev. B* **68**, 104107 (2003).
- [39] M. Rahaman, T. Imai, T. Sakamoto, S. Tsukada, and S. Kojima, Fano resonance of Li-doped $\text{KTa}_{1-x}\text{Nb}_x\text{O}_3$ single crystals studied by Raman scattering, *Sci. Rep.* **6**, 23898 (2016).
- [40] Y. Wu, F. Liang, X. Wang, J. Wang, H. Yu, and H. Zhang, Temperature dependent Raman spectroscopic study of Fano resonance in perovskite ferroelectric $\text{KTa}_{1-x}\text{Nb}_x\text{O}_3$ single crystal, *Opt. Mater. Express* **12**, 247 (2022).
- [41] A. Sassella, D. Braga, M. Campione, T. Ciabattoni, M. Moret, J. Parravicini, and G. Parravicini, Probing phase transitions and stability of organic semiconductor single crystals by dielectric investigation, *J. Appl. Phys.* **109**, 013529 (2011).
- [42] H. Fröhlich, *Theory of Dielectrics*, 2nd ed. (Clarendon, Oxford, 1958).
- [43] J. Parravicini, Thermodynamic potentials in anisotropic and nonlinear dielectrics, *Phys. B: Condens. Matter* **541**, 54 (2018).
- [44] J. Parravicini and G. Parravicini, Measuring state-of-order by dielectric response: a comprehensive review on Fröhlich entropy estimation, *Results Phys.* **28**, 104571 (2021).
- [45] V. Kochervinskij and I. Malyshkina, Dielectric spectroscopy of ferroelectric polymers, in *Organic Ferroelectric Materials and Applications* (Elsevier, Amsterdam, 2022), Chap. 9, pp. 263–355.
- [46] P. Tan, H. Tian, F. Huang, X. Meng, Y. Wang, C. Hu, X. Cao, L. Li, and Z. Zhou, Strain-Gradient-Controlled Disorder Dynamics in Chemically Substituted Ferroelectrics, *Phys. Rev. Applied* **11**, 024037 (2019).
- [47] J. Parravicini, L. Fornasari, E. DelRe, F. Marabelli, A. J. Agranat, and G. Parravicini, Evidence of double-loop hysteresis in disordered ferroelectric crystal, *J. Appl. Phys.* **127**, 184107 (2020).
- [48] J. Parravicini, M. Acciarri, A. Lomuscio, M. Murabito, A. Le Donne, A. Gasparotto, and S. Binetti, Gallium In-Depth Profile in Bromine-Etched Copper-Indium-Gallium-(Di)selenide (CIGS) Thin Films Inspected Using Raman Spectroscopy, *Appl. Spectrosc.* **71**, 1334 (2017).
- [49] M. Acciarri, A. Le Donne, S. Marchionna, M. Meschia, J. Parravicini, A. Gasparotto, and S. Binetti, CIGS thin films grown by hybrid sputtering-evaporation method: properties and PV performance, *Solar Energy* **175**, 16 (2018).
- [50] V. Shvartsman and D. Lupascu, Lead-Free Relaxor Ferroelectrics, *J. Am. Ceram. Soc.* **95**, 1 (2012).
- [51] G. Samara, The relaxational properties of compositionally disordered ABO_3 perovskites, *J. Phys.: Condens. Matter* **15**, R367 (2003).
- [52] G. Xu, J. Wen, C. Stock, and P. Gehring, Phase instability induced by polar nanoregions in a relaxor ferroelectric system, *Nat. Mater.* **7**, 562 (2008).
- [53] M. D. Fontana, A. Ridah, G. E. Kugel and C. Carabatos-Nedelec, The intrinsic central peak at the structural phase transitions in KNbO_3 , *J. Phys. C: Solid State Phys.* **21**, 5853 (1988).
- [54] M. V. Abrashev, A. P. Litvinchuk, M. N. Iliev, R. L. Meng, V. N. Popov, V. G. Ivanov, R. A. Chakalov, and C. Thomsen, Comparative study of optical phonons in the rhombohedrally distorted perovskites LaAlO_3 and LaMnO_3 , *Phys. Rev. B* **59**, 4146 (1999).
- [55] H. P. Soon, H. Taniguchi, and M. Itoh, Dielectric and soft-mode behaviors of AgTaO_3 , *Phys. Rev. B* **81**, 104105 (2010).
- [56] H. Taniguchi, M. Itoha, and D. Fu, Raman scattering study of the soft mode in $\text{Pb}(\text{Mg}_{1/3}\text{Nb}_{2/3})\text{O}_3$, *J. Raman Spectrosc.* **42**, 706 (2011).